Title
CHARACTERISATION OF INORGANIC MATERIALS

Author
Thomas, G.

Publication Date
1985-12-01

Lawrence Berkeley Laboratory
UNIVERSITY OF CALIFORNIA

Materials & Molecular Research Division

To be presented at the ICEM XIth International Congress on Electron Microscopy, Kyoto, Japan, August 31-September 7, 1986

CHARACTERISATION OF INORGANIC MATERIALS

G. Thomas

December 1985

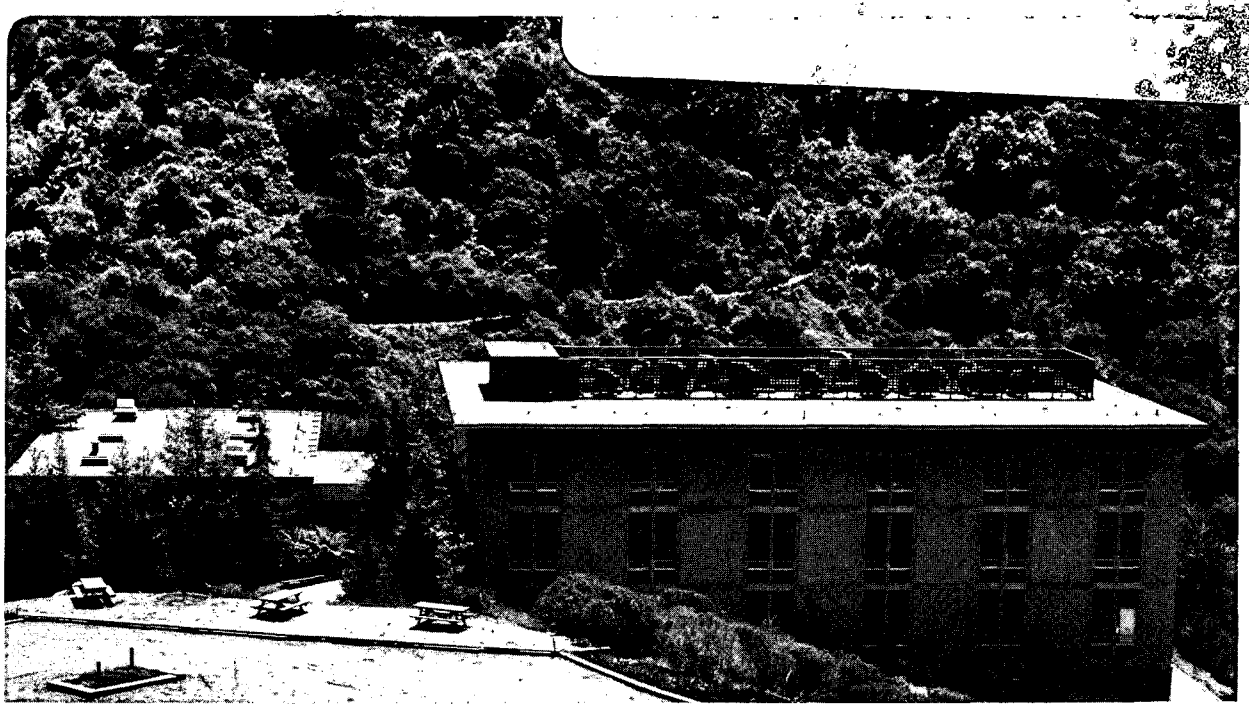

Prepared for the U.S. Department of Energy under Contract DE-AC03-76SF00098

DISCLAIMER

ICEM XIth INTERNATIONAL CONGRESS ON ELECTRON MICROSCOPY

KYOTO, JAPAN, AUGUST 31-SEPTEMBER 7, 1986

CHARACTERISATION OF INORGANIC MATERIALS

GARETH THOMAS

Professor, Department of Materials Science and Mineral Engineering, University of California, Berkeley, CA 94720

and

Scientific Director, National Center for Electron Microscopy

Materials and Molecular Research Division

Lawrence Berkeley Laboratory

Berkeley, CA 94720 USA

Although this paper is included in the Symposium on High Voltage Electron Microscopy, the emphasis here will be on examples from our research using the wide range of techniques available in modern electron microscopes. The general advantages of HVEM are now well known and need not be repeated.

Introduction: At the previous 1982 Congress it was clear that more and more research would involve high resolution techniques. The new generation of HV microscopes now allow imaging to better than 2Å point to point resolution and specially dedicated microscopes such as the Berkeley ARM installed in 1983 have proved 1.5Å interpretable resolution. However progress in quantitative analytical methods (including detection)seems slower. Without field emission guns and ultrahigh vacuum or controlled atmosphere chambers, the signal-detection system limits spatial resolution to about 600 Å and minimum detectable masses in the range 10^{-19} (Z 10 to 40) but simultaneous collection in EDX systems makes qualitative analysis quite routine. On the other hand energy loss spectroscopy whilst attractive for light element analysis, since the K edges are well separated, is difficult and time consuming (although parallel detection systems are in commercial development). The main problem is the need for thin, (500 Å or so) clean specimens otherwise multiple scattering and the high background completely obliberates resolvable spectra such as needed for C,N,O analyses in many materials systems. In many samples problems due to contamination from foil preparation and damage during microscopy examination remain paramount.

Ceramics: EELS is particularly useful in ceramics research for the detection of the light anions C,N,O, etc. One example is SiC sintered with the addition of carbon. While an optimum addition of carbon enhances the sintering process, an excess amount can impede densification. Electron microscopy and EELS have been used to identify excess carbon and its form in a sintered SiC compact. These results are shown in fig. 1. The detail of the near edge structure (bonding sensitive) shows the carbon to be graphitic.

Silicon nitride is another important ceramic, and attempts to produce dense and high temperature creep resistant silicon nitride by hot pressing or sintering using oxide additives have been fraught with the problems associated with the retention of intergranular glassy or partially crystallised phases. The identification of these features has been a notable triumph for electron microscopy. Figures 2a-d show examples of precipitation in Y-Al-Si-O-N glasses of a dendritic $Y_2Si_2O_7$ (y) phase from a glass which subsequently transforms to a different polymorph (Òphase) whilst the interdendritic glass enriches in Al and N as can be shown by EDXS using thin window detectors (insets in fig. 2c. The ARM images such as figs. 2c, 2d together with x-ray and CBD analyses are being utilized to understand the crystallisation and transition mechanisms.

Although γ-Fe_2O_3 particles have been widely used for several decades, the structure of this material remains unresolved mainly because the techniques involved in previous studies did not have the

resolution needed for localized information. Figure 3 shows primary CBED zone axis patterns of the γ-Fe_2O_3 particles. Since the internal structure of the zero-order discs in the CBED patterns cannot be seen, due to small particle size, the crystal symmetry must be determined from analysis of the high order Laue zone symmetry. From b,c,d, it can be seen that the <100>, <111>, and <110> zone axis patterns show the 4mm, 3m, and 2mm symmetries, respectively. Hence the point group can be unambiguously determined to be m3m with a ~25Å . This crystal symmetry also rules out all of the space groups proposed by previous investigators. This superstructure is a result of cation vacancy ordering and is observed as shown by the <110> CBED patterns in figs.3d and 3e, to gradually change to a disordered structure with lattice parameter of 8.33 Å under prolonged electron exposure.

In other oxide ceramics, considerable interest exists in mechanically strong, and tough composites of zirconia with various matrices. In our own program in collaboration with Dr. J. Moya (CSIC Spain), reaction sintered products yielding zirconia and mullite are being investigated. A typical micrograph is shown in fig. 4 with EDX data in figs. 5a,b. The significance here is the presence of Zr in mullite with Ti partitioning across the ZrO_2-mullite interface. HREM studies show the absence of glass at these interfaces. The situation is complex as the ZrO_2 may be ordered and detailed CBD studies of ZrO_2 (partially stabilized with various additives), and mullite, e.g. fig. 6, is under way.

Metals, semiconductors: Very high resolution studies are now being widely made and the problems of interfaces (free surfaces, boundaries, layered structures interphase interfaces etc.,) are common to all inorganic materials. One example, and one which illustrates the excellent resolution and contrast obtained in the ARM is shown in fig. 7 which is an image of needles of Ge precipitated in a dilute Al-Ge alloy. At least three primary orientation relationships were observed; (a) {111} Ge || {100} Al, (b) {100} Ge || {100} Al and (c) {110} Ge || {110} Al. In fig. 7 the two longest flat facets are {111} Ge planes parallel to {310} Al while the shorter facets are another set of {111} Ge planes parallel to {100} Al. The primary orientation relationship of this precipitate and the one most frequently found is that with monoclinic 2/m symmetry. The shape of this particle also has approximately 2/m symmetry along its axis, but the perfect symmetry is disrupted by the internal twins. The twins are in a secondary orientation relationship because their twin plane is the {111} Ge plane that is parallel to {310} Al. Note that the corresponding interfaces with the matrix are atomically flat on the Ge side, leading to a stepped appearance on the Al side.

A very similar image to that of fig. 7 is fig. 8 which is an Al-GaAs contact prepared by MBE. In this work domains elongated parallel to the GaAs interface were observed when the interface was "rough" but when atomic flat surfaces are obtained domains were not present (fig. 8). These effects have been interpreted in terms of exchange reactions between Al and As. Such information is critical to the understanding of such Schottky contacts and to their processing. Finally atomic resolution imaging may, with proper interpretation and imaging

conditions, allow atomic discrimination to be obtained. Figure 9 is an example of pear shaped images in a [110] projection of GaAs. The shape is due to the scattering differences between Ga and As at 1.4Å separation. Such detail is needed for research on defects, e.g. "antisites".

As new HVEM instruments become available with full analytical and CBD capabilities electron microscopy will continue to be essential to characterize, better understand, and develop materials.

ACKNOWLEDGEMENTS

This work was supported by the Director, Office of Energy Research, Office of Basic Energy Sciences, Materials Sciences Division of the U.S. Department of Energy under Contract No. DE-AC03-76SF00098. Ceramics research was supported by NSF under Contract No. DMR 83-1317239. The work reported here is all based on current research of my colleagues and students as indicated in the figure captions.

FIGURE CAPTIONS

Fig. 1(a). Image of partially dense SiC with excess carbon. (b) ELS spectra from carbon region; (c)(d)(e) Standard ELS spectra from amorphous, graphitic and diamond carbon forms (Courtesy B. Dalgleish).

Fig. 2. (a) SEM, (b) TEM of dendritic nucleation in a Y-Si-Al-O-N glass, (c) ARM glass-silicate interface, (d) ARM showing three crystallisation products: note partitioning of Al and N to the glass, but not in crystalline phases.

Fig. 3. (a) Bright and dark field image of an isolated γ-Fe_2O_3 particle showing it is a single crystal. (b), (c), and (d) are <100>, <111>, and <110> CBED zone axis patterns, respectively. (f) <110> CBED pattern of the disordered structure resulting from electron beam damage.

Fig. 4. 350 kv; zirconia particles in mullite produced by reaction sintering. The intergranular zirconia is monoclinic whereas the intragranular is retained tetragonal when less than 0.3μ diameter.

Fig. 5. EDX spectra from zirconia and surrounding mullite.

Fig. 6. 1 mev ARM image of mullite [001] (Courtesy of G. van Tendeloo); The CBD pattern shows the dynamical absences (dark bars) corresponding to the a and b glide planes of the Pbam space group. (Courtesy T.A. Bielicki).

Fig. 7. Precipitate of Ge in Al (ARM image at 1 mev). Notice structural twinning parallel to broad faces. (Courtesy U. Dahmen, K.H. Westmacott).

Fig. 8. 1 mev ARM cross section image of Al/GaAs interface (100)Al|| [110]G; [010]Al||[110]G. (Courtesy Z. Lilienthal-Weber and R. Gronsky).

Fig. 9. Atomic resolution image of the pear shaped GaAs atomic configuration at 1.4 Å spacing. (Courtesy R. Gronsky).

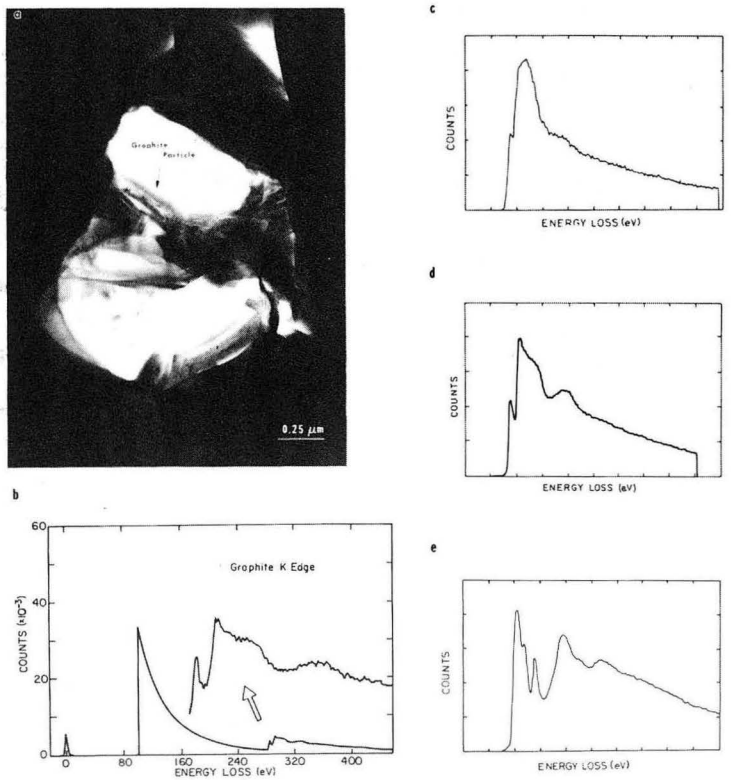

XBB 858-7008

Fig. 1

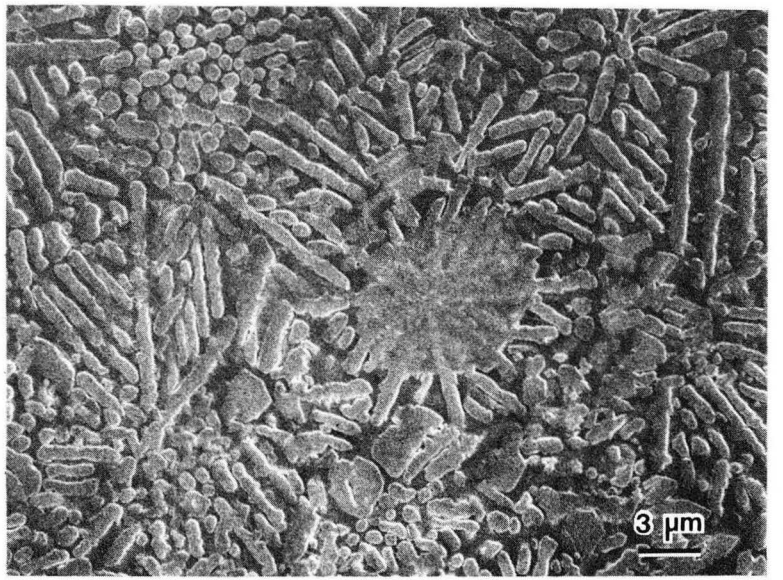

XBB 850-10032

Fig. 2a

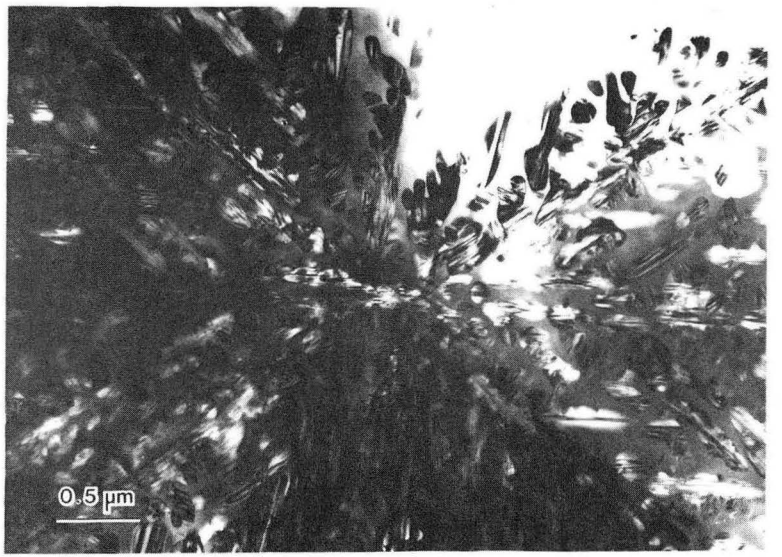

XBB 854-2600

Fig. 2b

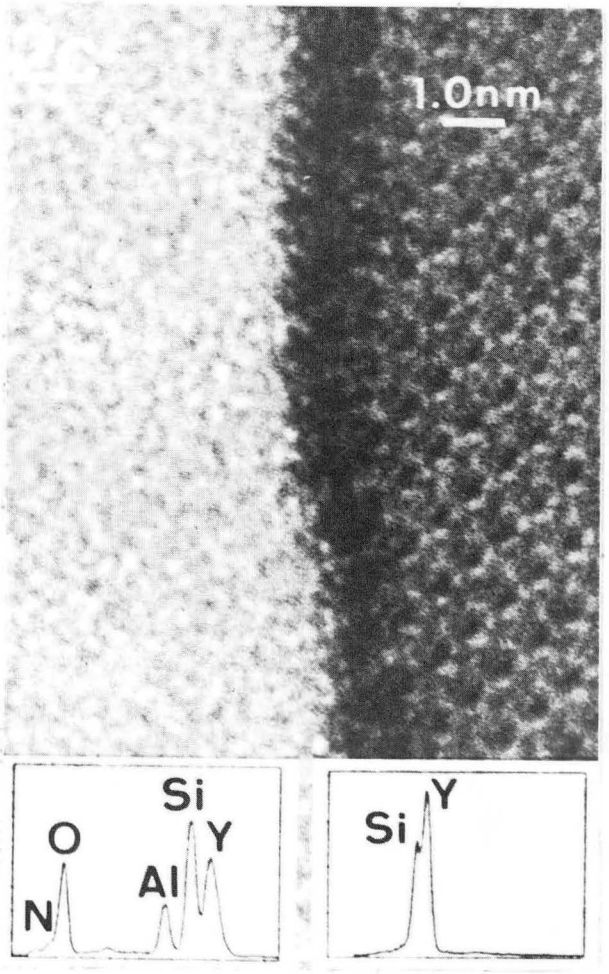

XBB 865-4146

Fig. 2c

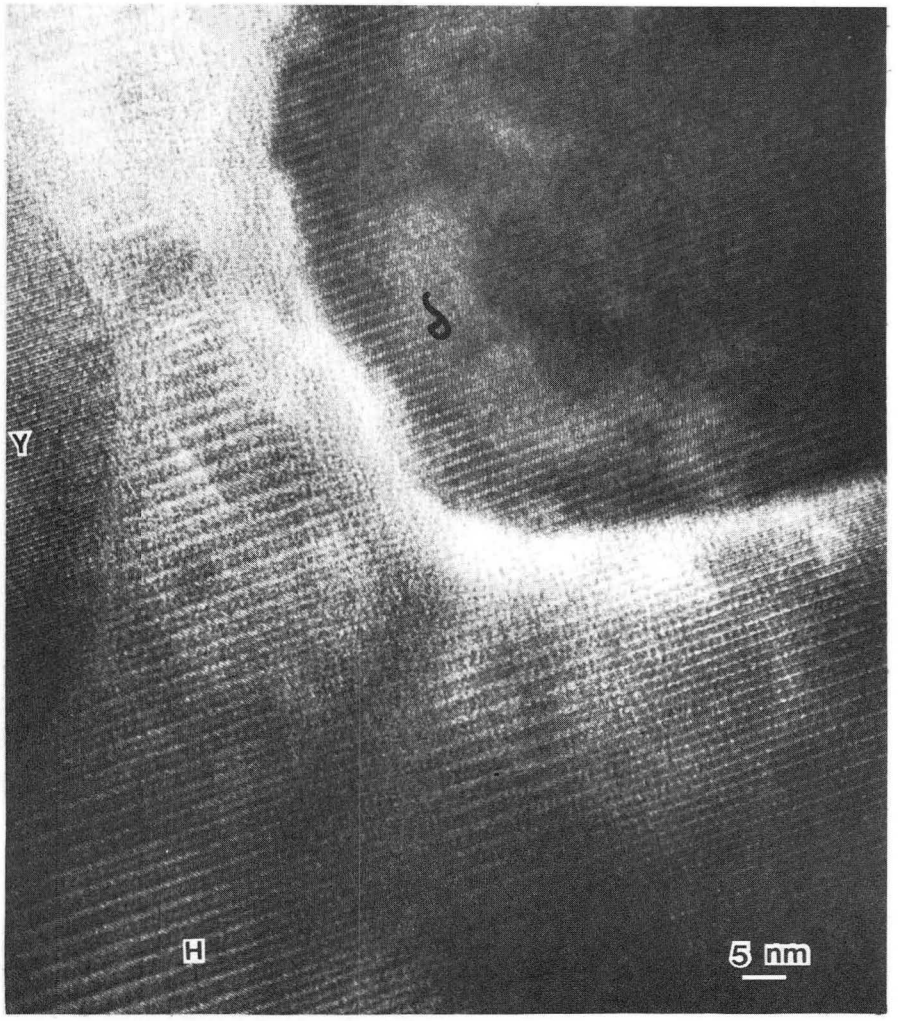

XBB 850-8236

Fig. 2d

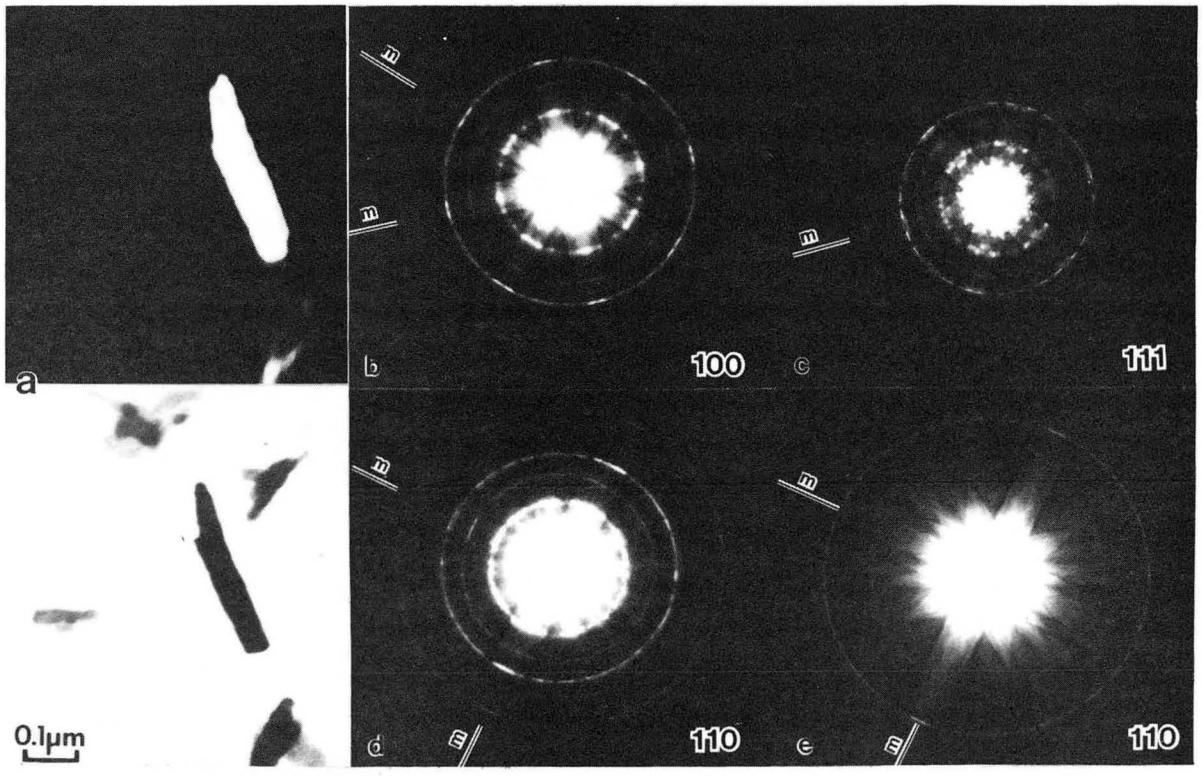

XBB 854-2965 XBB 863-1544

Fig. 3

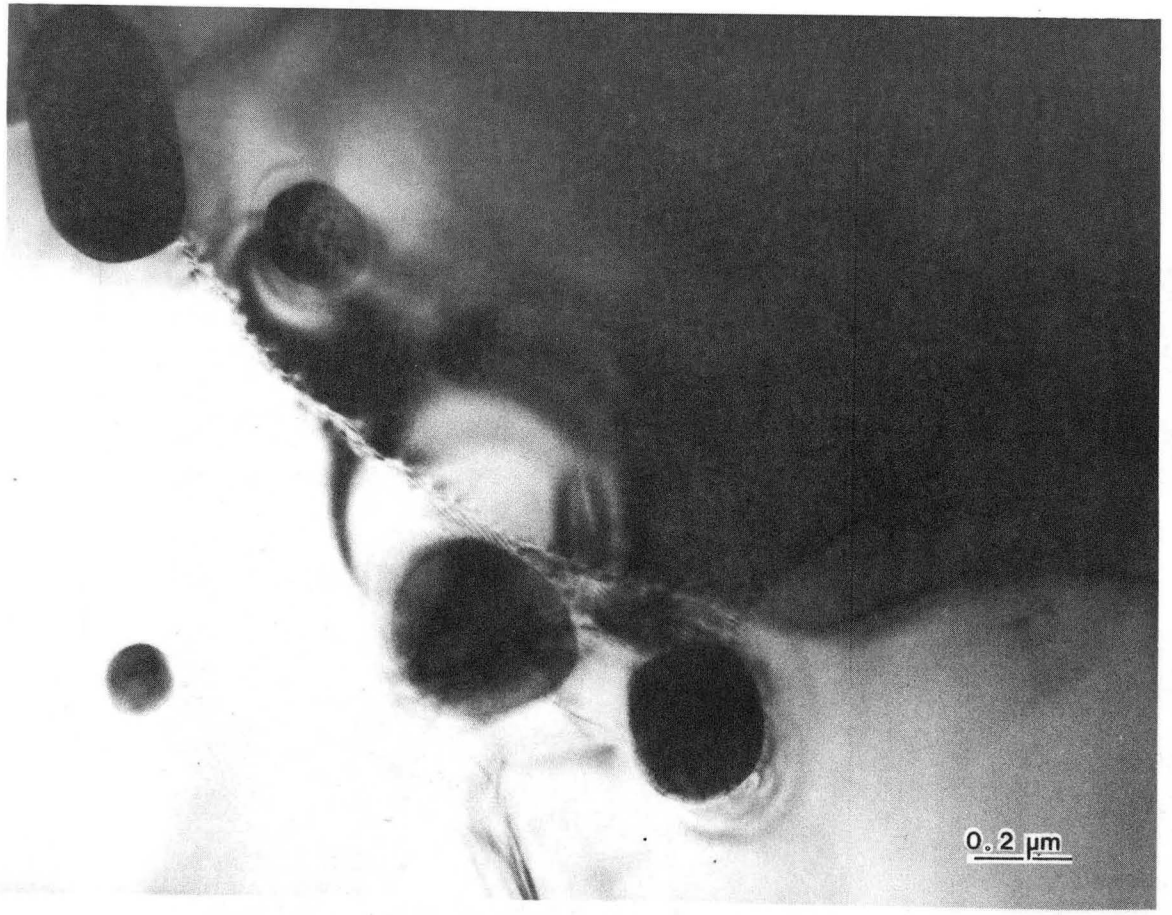

XBB 862-1005

Fig. 4

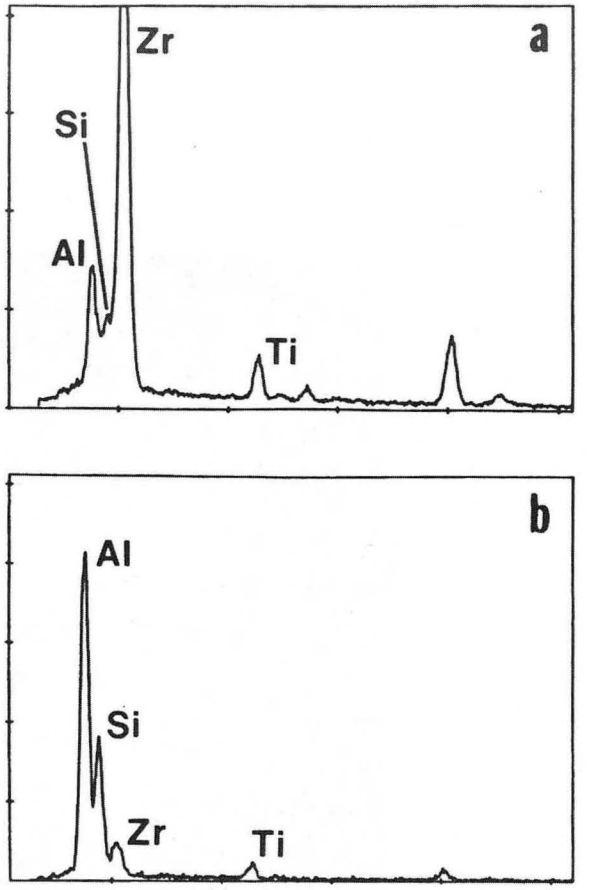

XBL 865-1698

Fig. 5

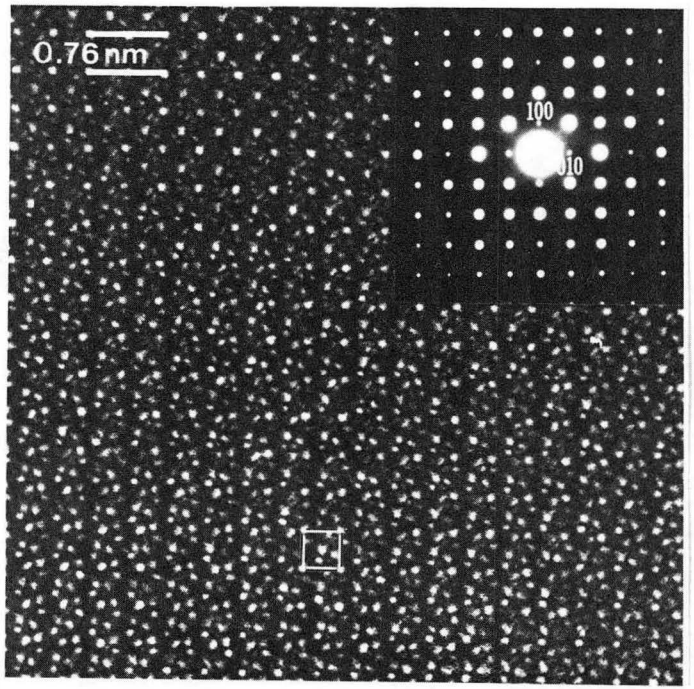

XBB 848-5777

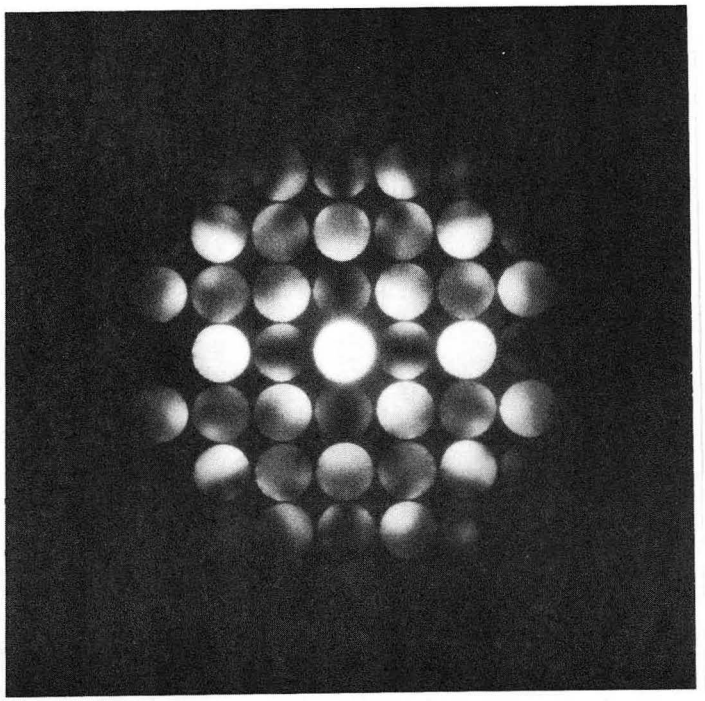

XBB 857-5440

Fig. 6

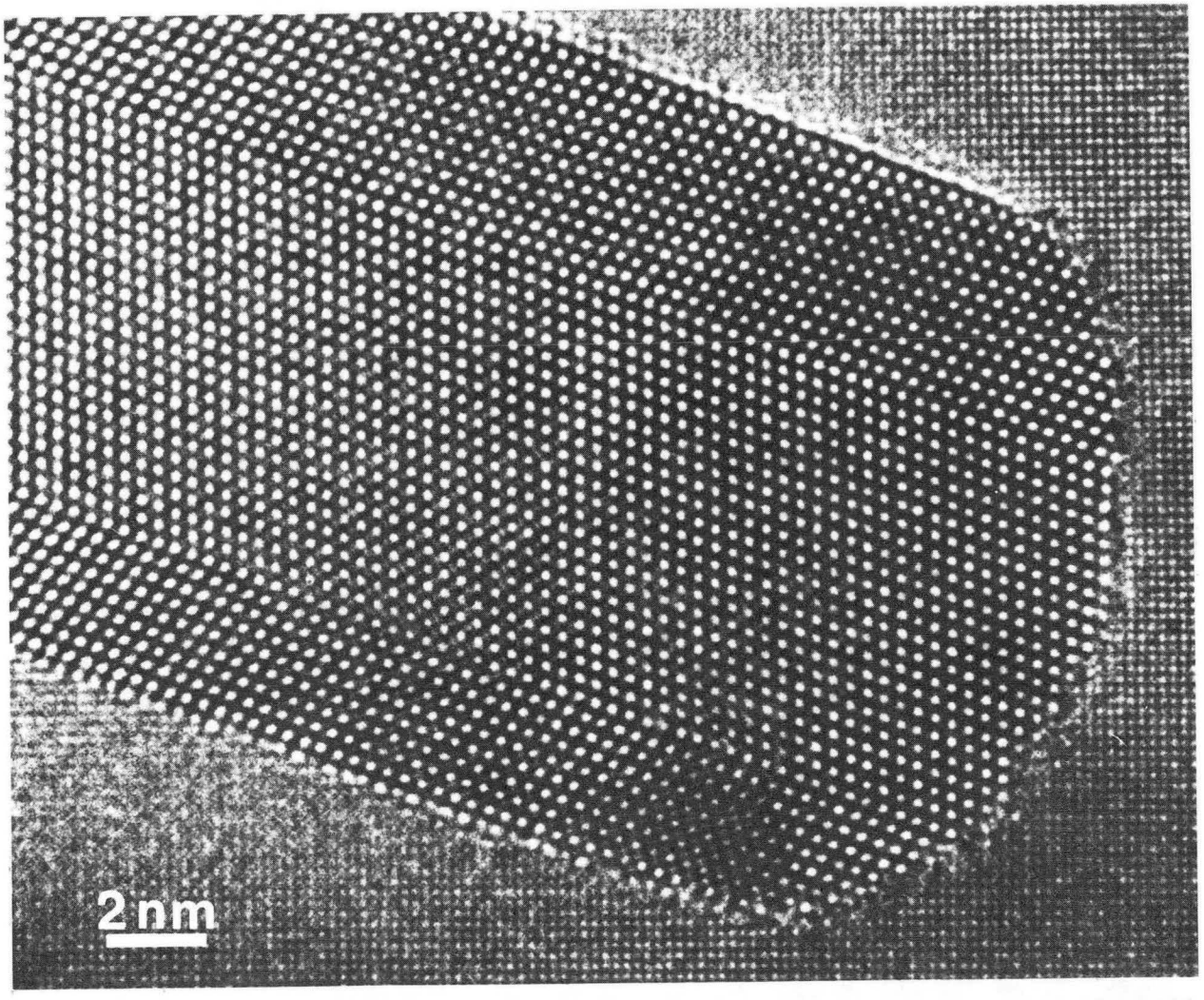

XBB 865-4145

Fig. 7

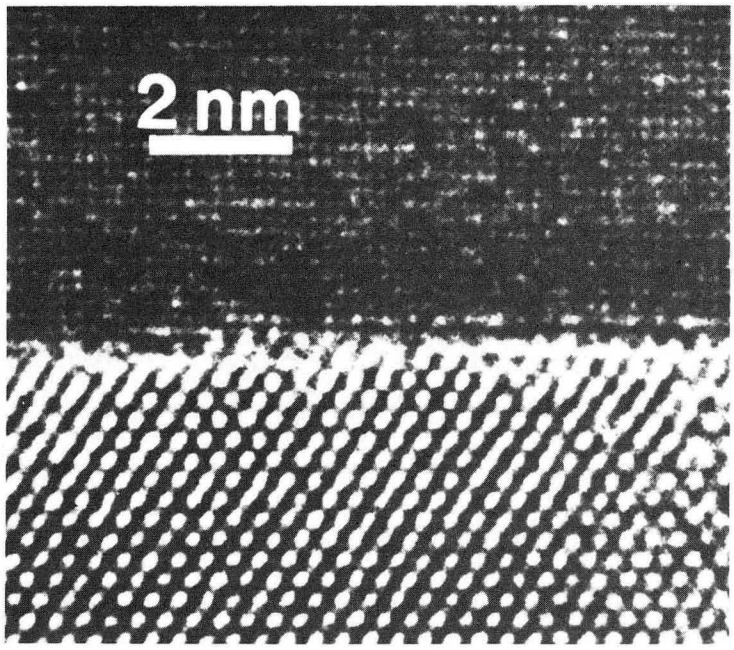

XBB 865-4144

Fig. 8

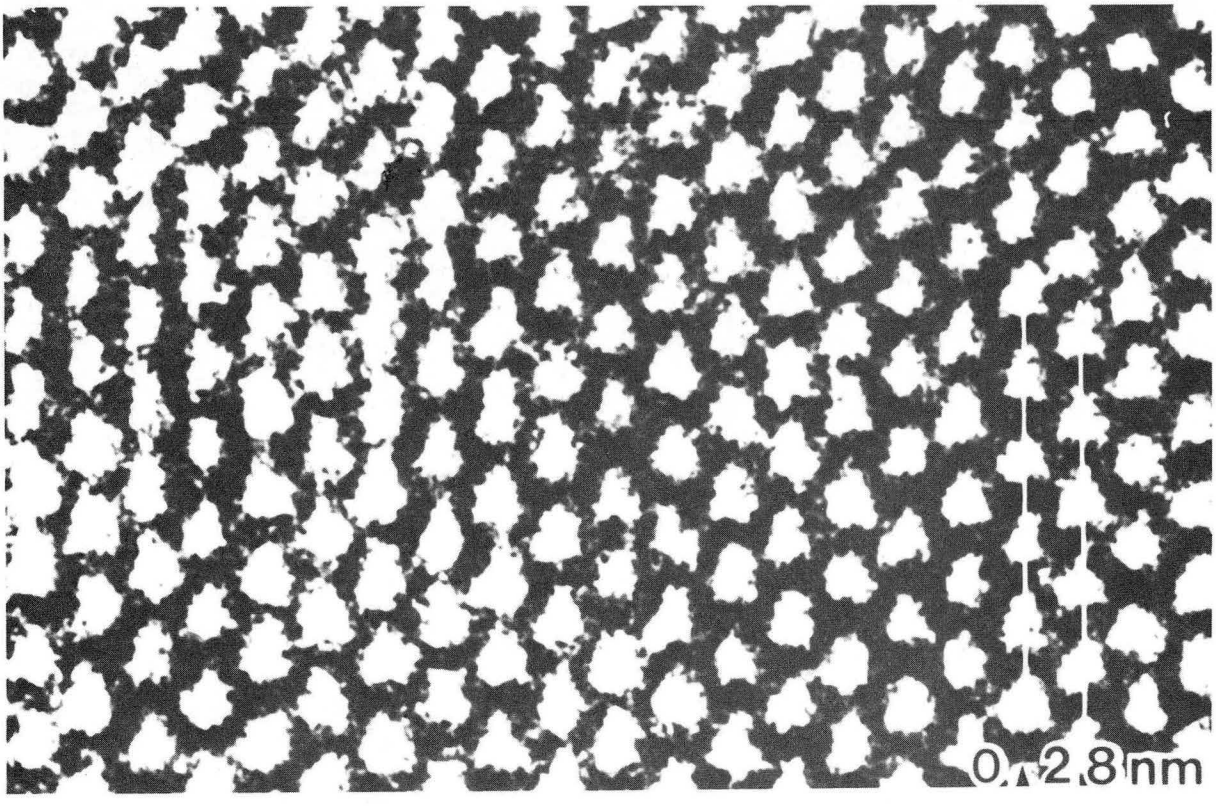

XBB 865-4143

Fig. 9

LAWRENCE BERKELEY LABORATORY
TECHNICAL INFORMATION DEPARTMENT
UNIVERSITY OF CALIFORNIA
BERKELEY, CALIFORNIA 94720